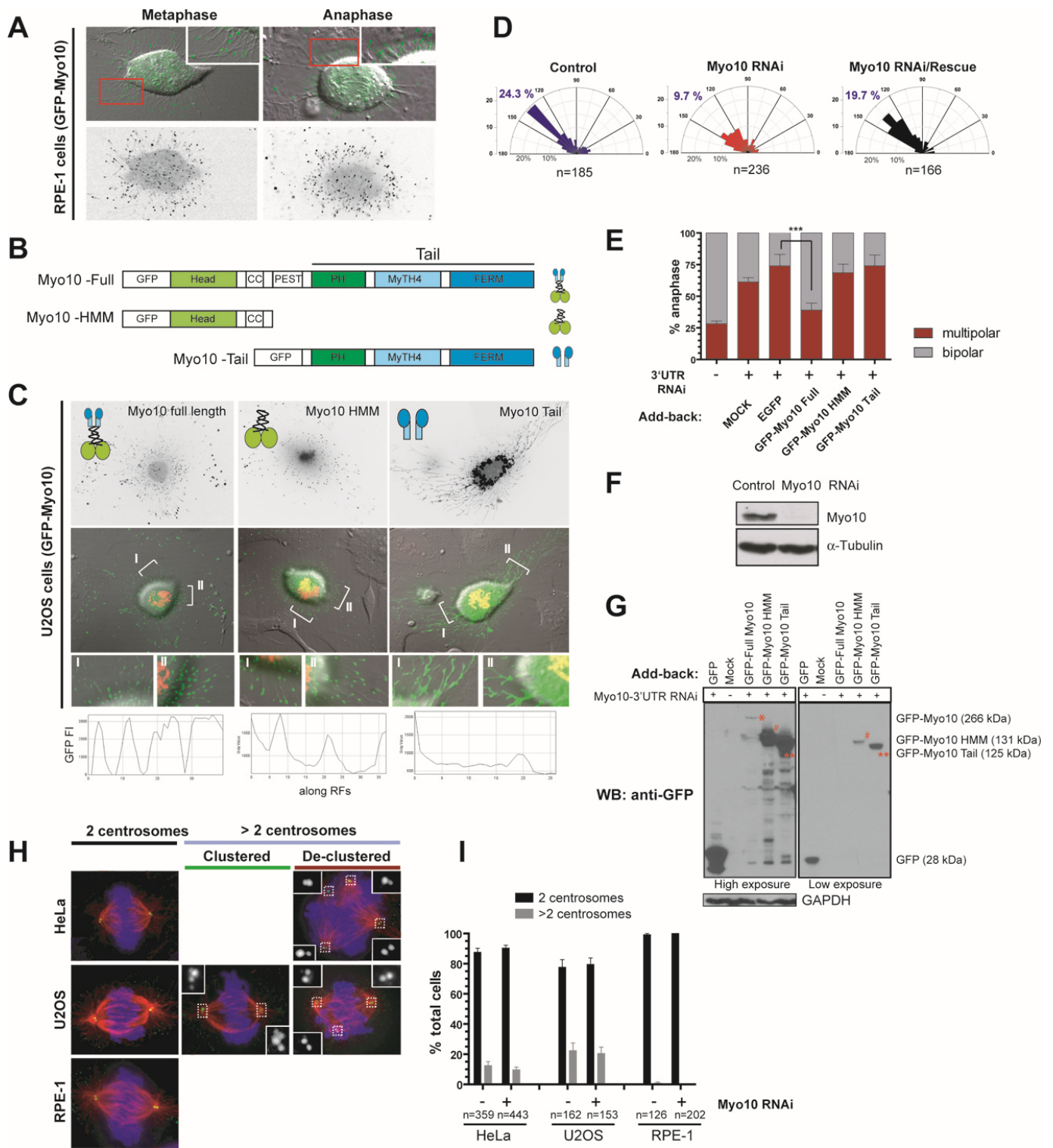


Developmental Cell

Supplemental Information

**Direct Microtubule Binding by Myosin-10  
Orients Centrosomes toward Retraction Fibers  
and Subcortical Actin Clouds**

Mijung Kwon, Maria Bagonis, Gaudenz Danuser, and David Pellman



**Figure S1 (related to Figure 1). The Motor Domain of Myo10 Is Sufficient for Retraction Fiber (RF) Localization; the Motor and Tail Domains Are both Required for Centrosome Positioning; Loss of Myo10 Does Not Induce Centrosome Fragmentation.**

(A) Myo10 localizes to retraction fibers (RFs) during metaphase and anaphase in RPE-1 cells. GFP-Myo10 (bottom, inverted images) is overlaid on the DIC (RFs) images (insets, high magnification images of red box regions).

(B) Schematic of the Myo10 domain structure and of the GFP-tagged Myo10 constructs used for localization (C) and functional assays (E-G). Domains: Head, motor domain; CC, coiled coil; PEST, proline (P) glutamate (E) serine (S) and threonine (T) domain; PH, pleckstrin homology domain; MyTH4, myosin tail homology 4; FERM, four-point-one, ezrin, radixin, moesin domain.

(C) The motor domain, but not the tail domain, is required for localization of Myo10 to RFs. Images show U2OS cells expressing RFP-H2B and the indicated Myo10 constructs. Top panels: inverted images showing the GFP-Myo10 signal. Middle panels: merged images of DIC (RFs), GFP-Myo10 and RFP-H2B in mitotic cells. Bottom panels: high magnification images of RFs (in regions I and II) and the representative fluorescence line scans of GFP-Myo10 along RFs.

(D) Requirement of Myo10 for spindle orientation in U2OS cells expressing GFP-H2B on fibronectin (FN)-L patterns. Angular ( $\alpha$ ) distribution of the cell division axis in the indicated conditions (Fig 1C) was used to obtain the percentage of cells that were dividing with a median angle of 135 degrees ( $\alpha = 135 \pm 10$ ) shown in Figure 1D.

(E) Both the motor and tail domains of Myo10 are required for complementation of centrosome clustering defects in cells depleted of endogenous Myo10. The percentage of anaphase cells with multipolar or bipolar divisions are shown in control cells (-) or cells depleted of endogenous Myo10 (+, 3'UTR RNAi) that were transfected with GFP (negative control) or the indicated Myo10 constructs. \*\*\* $p < 0.002$ , non-parametric Student's t-test. Data represents mean of 3 experiments  $\pm$  s.e.m.

(F) Western blots showing the knockdown of Myo10 in U2OS cells.

(G) Western blots showing protein levels of rescue-incompetent Myo10 mutant constructs (Myo10 HMM and Tail) probed with anti-GFP antibodies. Blots with high (left) and low (right) exposure. \*, GFP-Myo10; #, GFP-Myo10 HMM; \*\*, GFP-Myo10 tail.

(H-I) Myo10 depletion does not affect centriole number or centrosome integrity in the cell lines used in this study.

(H) Representative immunofluorescence images showing centrin (green),  $\alpha$ -tubulin (red), and DNA (Hoechst, blue). Insets: higher magnification of centrin images in boxed regions. Note that RPE-1 cells do not have extra centrosomes, and that HeLa cells cannot cluster extra centrosomes.

(I) Myo10 inhibition does not induce centrosome amplification in the cell lines used in the study. Note: We observed no centriole fragmentation, identified by a single centrin focus, nor spindle pole fragmentation, identified by ectopic spindle poles ( $\alpha$ -tubulin-positive but without centrioles), after Myo10 depletion in any of the cell lines.

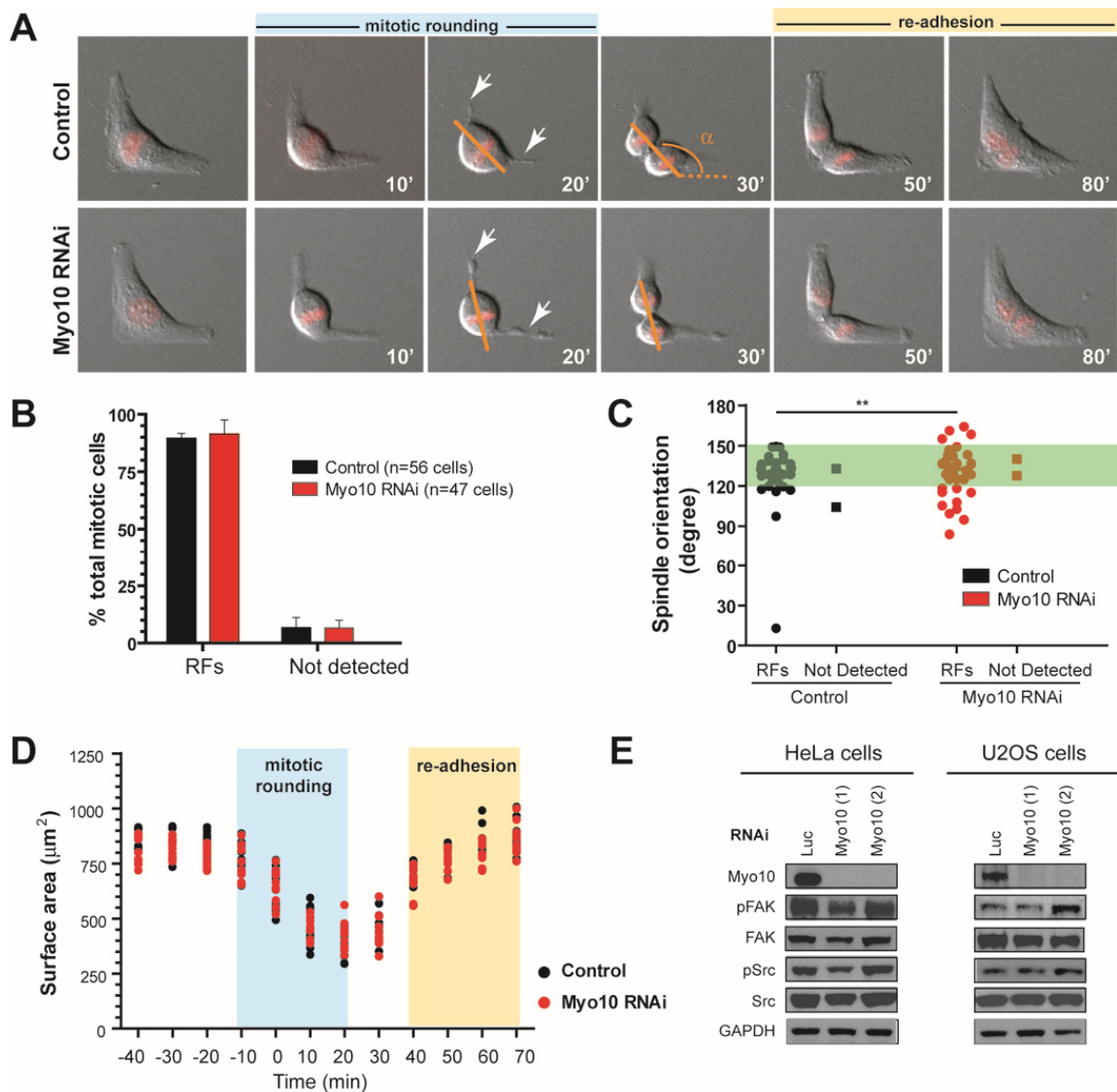


**Figure S2 (related to Figure 2). Normal Retraction Fibers, Cell Adhesion and Mitotic Cell Rounding in Myo10-Depleted Cells despite Abnormal Spindle Orientation.**

(A-D) Myo10-depleted RPE-1 cells exhibit well-defined retraction fiber (RF) regions and proper mitotic rounding, despite the presence of spindle orientation defects.

(A) Still images of live RPE-1 cells that express RFP-H2B dividing on FN-L patterns. Time: minutes from NEBD ( $t=0$ ). Orange lines: cell division axis. Arrows: RF regions.

(B) Myo10 depletion does not affect the percentage of cells with RFs. Data represents mean of 3 experiments  $\pm$  s.e.m. Note:  $\sim 4\%$  of cells were not scored for each sample because the putative RF region was ambiguous or out of focus.

(C) Myo10-depleted cells with spindle orientation defects (outside of green area deviating from  $120 < \alpha < 150$ ,  $**p < 0.05$ , non-parametric Student's t-test, 2 experiments  $\pm$  s.e.m) nevertheless have normal-appearing RFs. Quantitation of angular ( $\alpha$ ) distribution of cell division axis as in (A).

(D) No detectable defects in mitotic rounding and re-adhesion of Myo10-depleted cells. Mitotic cell rounding was quantified from live RPE-1 cells dividing on FN-L patterns as shown in (A). Each dot is an individual cell ( $n=10$  cells per condition from 2 experiments).

(E) Western blots showing comparable levels of activation of FAK and Src in HeLa and U2OS cells depleted of Myo10 using two independent siRNAs. Luc: control siRNA.



(K1647/K1650) that have been shown to directly bind to tubulin tails [\* in red box, (Hirano et al., 2011; Wei et al., 2011; Wu et al., 2011)].

(B) Comparable protein expression of mCherry-tagged Myo10 constructs used in siRNA-rescue experiments. Western blots were probed with anti-Myo10 antibodies.

(C) Requirement of Myo10 microtubule-binding for spindle orientation. Spindle orientation analysis was done as in Figures 1C-D for Figure 3C.

(D) Requirement of Myo10 microtubule-binding, but not its cargo-binding, for centrosome clustering. Left: Schematic of rescue experiment. Right: The percentage of multipolar or bipolar anaphases (GFP-H2B imaging) was scored in cells that expressed the indicated mCherry constructs (\*\* $p < 0.05$ , non-parametric Student's t-test, 3 experiments  $\pm$  s.e.m.). In this assay,  $\sim 12$ - $14$  h of doxycycline treatment led to  $\sim 85$ - $90\%$  of cells with extra centrosomes, as confirmed by centrin staining and spindle multipolarity induced by HSET RNAi (Kwon et al., 2008). Note: the modest difference in absolute numbers between results of this assay and that in Figure 7G is because in this experiment we used a longer time of Plk4 induction (See Supplemental Methods for details), which results in a higher initial frequency of cells with centrosome amplification; the experimental results shown in Figure 7G had  $\sim 70\%$  of cells with extra centrosomes.

(E) Model: Electrostatic interaction between positively charged K1647/K1650 residues of Myo10 and negatively charged tubulin tail directly links microtubule lattice and actin to position centrosomes.

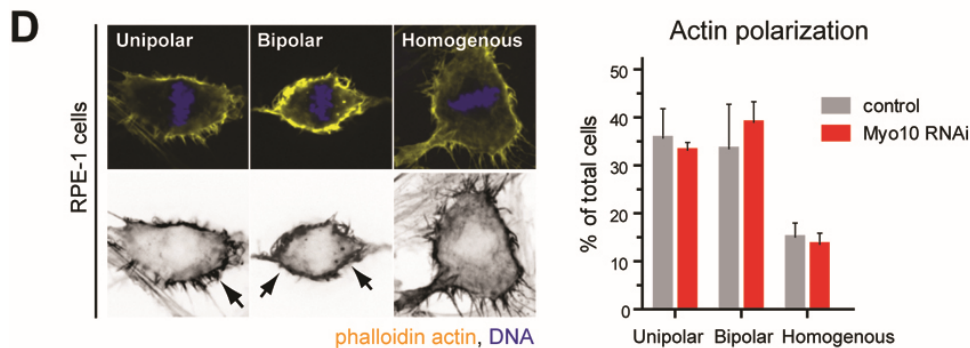
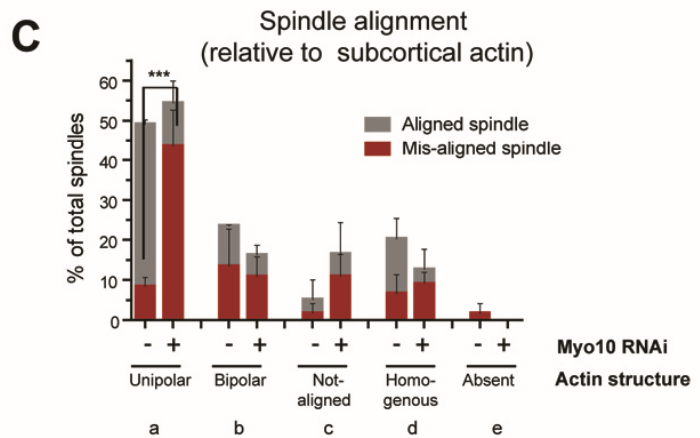
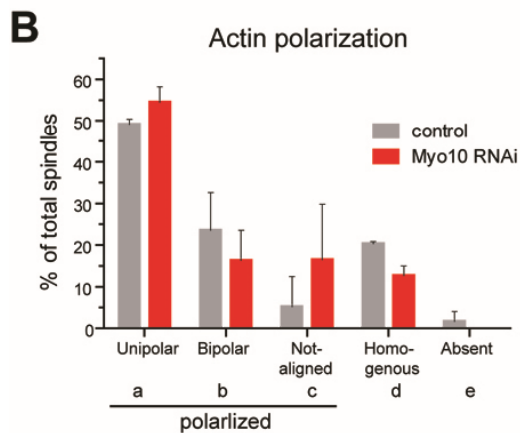
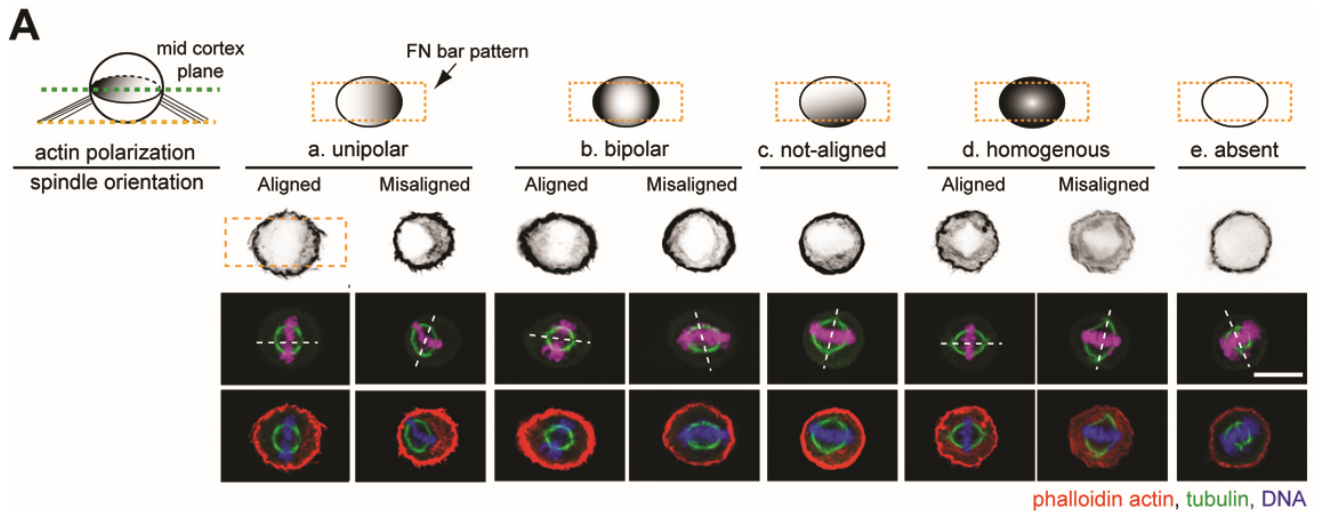


**Figure S4 (related to Figure 4). Myo10 Is Required to Orient Spindles Relative to Subcortical Actin Clouds.**

(A-C) Requirement of Myo10 for spindle orientation to the subcortical actin clouds in HeLa cells plated on FN-bar patterns.

(A) Characterization of the morphology of subcortical actin, including the rare categories where subcortical actin is asymmetric but not aligned with the pattern, and where subcortical actin is not detectable. Top: Schematic of the classification scheme used for subcortical actin polarity (Dark shade, subcortical actin concentration zone; yellow box area, adhesion surface of FN-bar patterns). Bottom: Representative

immunofluorescence images of HeLa cells quantified in (B-C). Cells were plated on bar patterns, fixed, and stained for phalloidin actin, tubulin, and DNA. The actin polarization pattern (inverted images) and spindle orientation axis (dotted white lines) are shown in the top and middle panels, respectively. Scale bar, 10  $\mu$ m.

(B) Depletion of Myo10 has no significant effect on the positioning of subcortical actin relative to sites of adhesion. The percentage of metaphase cells that exhibit polarized (unipolar, bipolar, and not aligned relative to adhesion geometry), homogenous, or undetectable subcortical actin is shown for Myo10 RNAi and the control.

(C) Myo10 is required to orient spindles relative to unipolar subcortical actin clouds (\*\*p<0.001, non-parametric Student's t-test, 3 experiments  $\pm$  s.e.m).

(D) Depletion of Myo10 has no significant effect on the accumulation of subcortical actin clouds in RPE-1 cells. Left: Subcortical actin clouds in cells plated on FN-coated plates, and stained for phalloidin actin (yellow) and DNA (blue). Right: The percentage of metaphase cells that exhibit unipolar, bipolar, or homogenous subcortical actin is shown for Myo10 RNAi and the control.



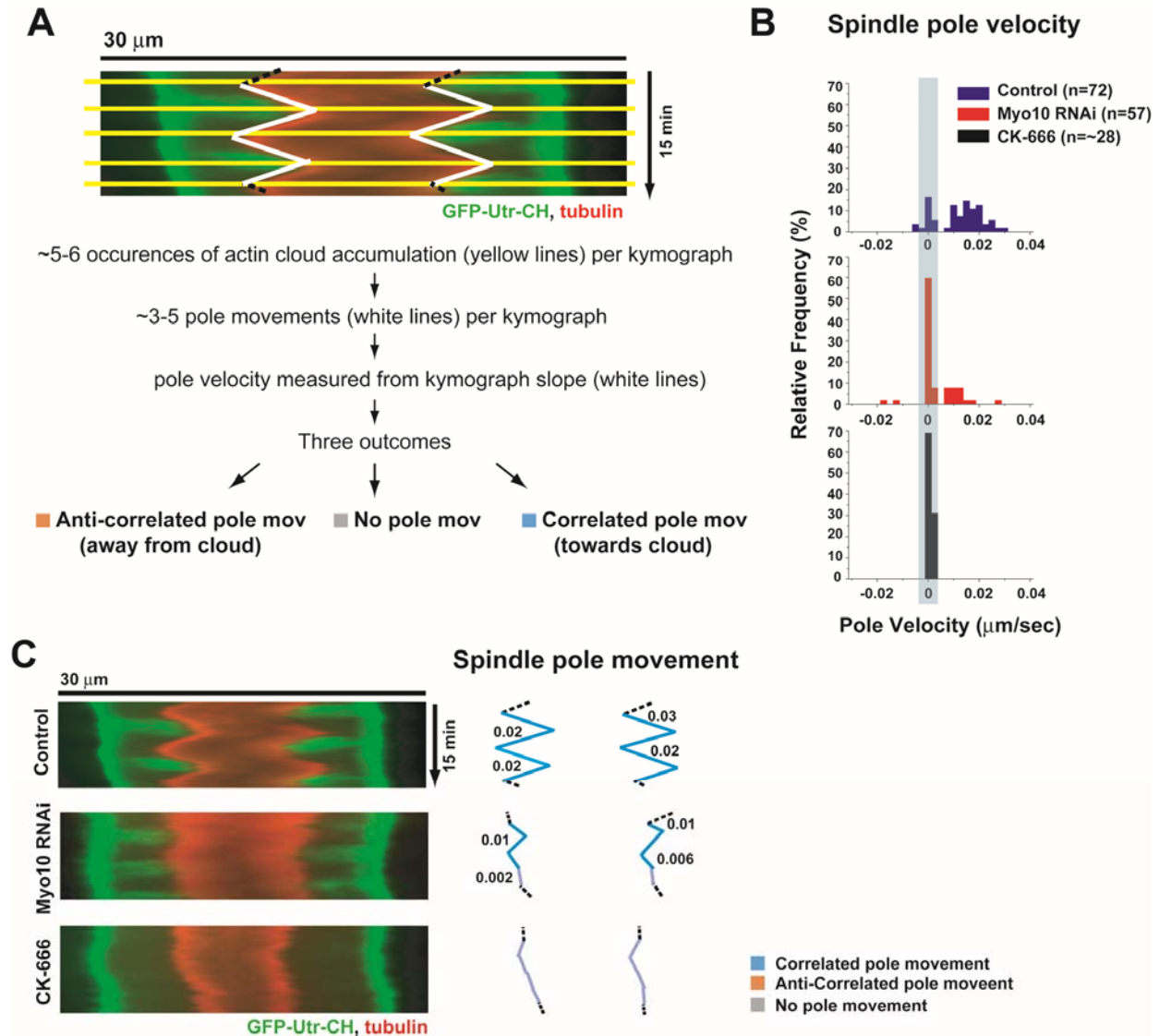


**Figure S5 (related to Figure 5). Requirement of Myo10 for Actin Cloud-Mediated Pulling Forces on Centrosomes during Metaphase Spindle Oscillations.**

(A) Schematic for the quantitation of actin cloud assembly dynamics and spindle pole movement relative to actin clouds shown in Figure 5B. Spindle pole movements relative to the regions of actin cloud accumulation were classified as correlated (blue, pole moves towards actin clouds), anti-correlated (orange, pole moves against actin clouds) or no (grey) movement. Significant pole movement was defined as a velocity that is more than 20% of the mean velocity measured in the control sample (mean=0.0125  $\mu\text{m}/\text{sec}$ ), based on the observed movements after Arp2/3 complex inhibition in (B).

(B) A decrease in spindle pole movements towards actin clouds in Myo10-depleted cells. Histogram of pole velocity toward (+) or against (-) actin clouds in indicated conditions (3 experiments). No movement (<0.0025  $\mu\text{m}/\text{sec}$ , 20% of mean control value) is indicated by the grey box.

(C) Kymographs of actin clouds (green) and spindle pole (red) from the cells shown in Figures 5A-B in indicated conditions. Right: Representative traces of pole movements in kymographs (left) are color-coded according to the pole velocity classification in (A-B).

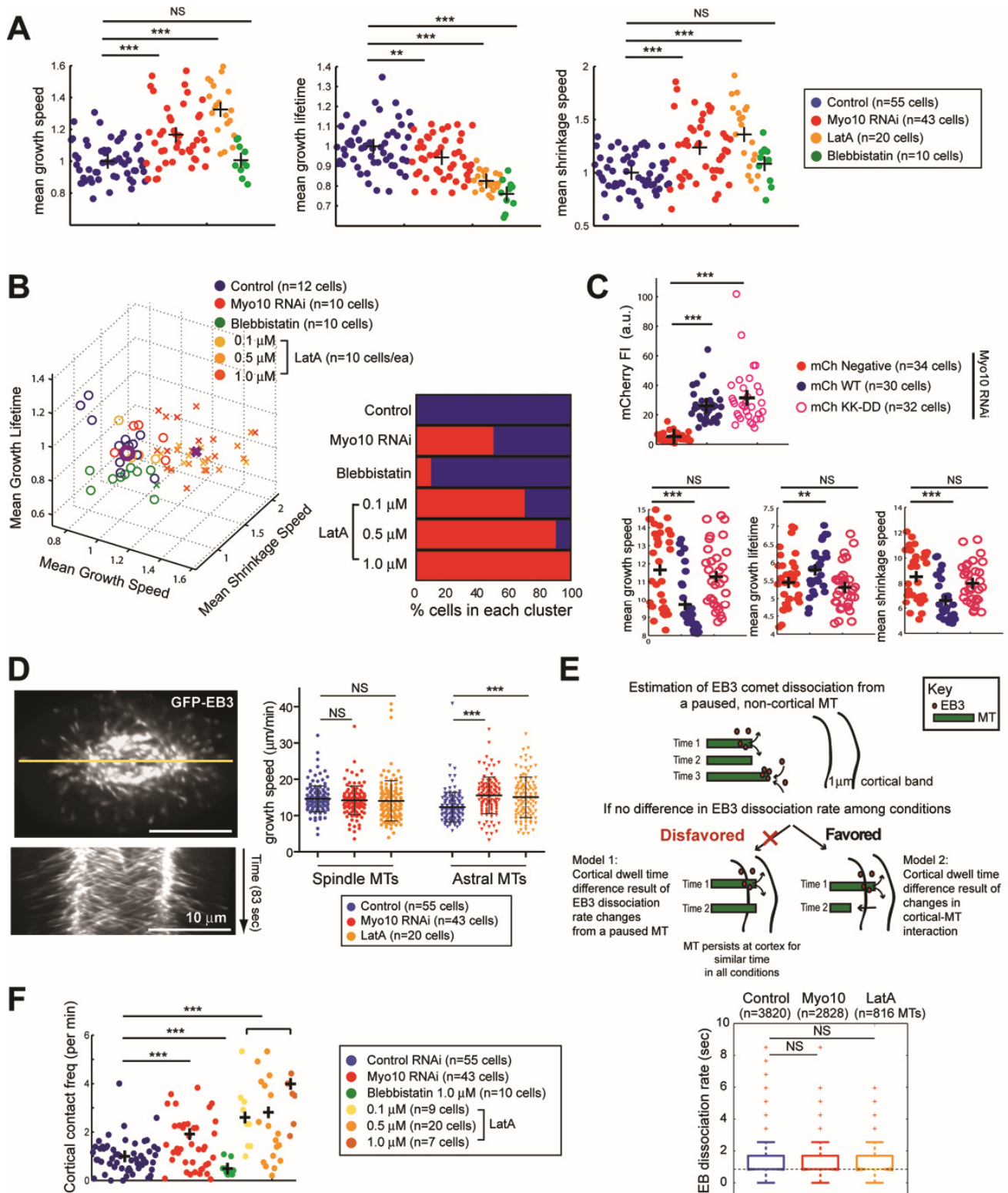


**Figure S6 (related to Figure 6). Myo10 and Actin Suppress Cortical Microtubule Dynamicity Prior to Anaphase.**

(A) Individual parameters of microtubule (MT) dynamics in control, Myo10-depleted, actin-disrupted (LatA treatment), or myosin II-inhibited (blebbistatin treatment) RPE-1 cells expressing GFP-EB3 (shown in Fig 6B). Each data point represents the average value for a given MT parameter from the entire astral MT population of each cell. The data are displayed as 2 dimensional (D) plots (unlike the 3D graph in Fig 6B) for visualization of differences between the samples for the individual parameters. Black crosses indicate the means for neighboring samples (Permutation test of the means, \*\*\* $p < 0.0001$ , \*\* $p < 0.02$ ).

(B) The effect of Myo10 on MT dynamics is distinct from a general disruption of cytoskeletal tension. Left: 3D plot of normalized mean MT growth speed, shrinkage speed, and growth lifetime, obtained from control cells (blue), cells depleted of Myo10 (red), or cells treated with blebbistatin (green) or different concentrations of LatA (different shade of yellow). Clustering of the data identified two distinct populations of cells that display highly (X) or less (O) dynamic MTs. Right: Unlike the effect of Myo10 knockdown, decreased myosin II-mediated contractility does not increase the percentage of cells with highly dynamic MTs (red). The relative percentages of cells that fall within the highly dynamic MT (red) or less dynamic MT (blue) category are shown for each condition.

(C) Requirement of Myo10 MT-binding for astral MT dynamics regulation. Top: Comparable expression (mCherry fluorescence intensity) of wild-type Myo10 or MT-binding (KK-DD) mutant used in the rescue experiment shown in Figure 6D (\*\*\* $p < 0.0001$ , permutation test of the means, 2 experiments). Bottom: Individual parameters of MT dynamics are displayed as 2D plots (from the 3D graph in Fig 6D). Permutation test of the means, \*\*\* $p < 0.0001$ , \*\* $p < 0.05$ .

(D) Myo10 depletion or actin disruption does not have a significant effect on MT growth speeds within the spindle. Left top: Single focal plane GFP-EB3 image of metaphase cell used for measurement of MT growth speed. Left bottom: Kymograph of the line generated along the long axis of spindle (horizontal and vertical scale bars represent 10  $\mu\text{m}$  and 1.4 min). Right: MT growth speed within the spindle and astral MTs quantified from the kymographs in indicated conditions (\*\*\* $p < 0.0001$ , non-parametric Student's t-test). Measurements sampled from the same 5 experiments shown in Fig 6B (error bars indicate s.e.m).

(E) The Myo10- or actin-dependent decrease in cortical dwell time is not the result of generally faster EB3 dissociation from the plus-ends of MTs. To determine whether Myo10 RNAi or LatA treatment affected EB3 dissociation from MT ends independent of cortical interaction, we measured the lifetime of EB3 on paused MTs outside the cortical region (see scheme and Supplemental Methods). The box plots show that the median EB3 dissociation rate is unchanged by Myo10 RNAi or LatA treatment (NS, permutation test of the medians, same 5 experiments shown in Figs 6B-C, E), which contrasts sharply with the data in Figure 6E where Myo10 RNAi or LatA treatment significantly affect EB3 comet cortical dwell time. Although there was no significant difference when the median values for Myo10 RNAi or LatA treatment are compared with the controls, there was a slight ( $\sim 0.2$  sec) but significant decrease in EB comet lifetime after Myo10 RNAi or LatA treatment when the mean values are compared ( $p < 0.01$  using a permutation test of the means). We attribute this difference to outlier measurements and a deviation from normality in these data (confirmed via Anderson-Darling tests) relative to the per cell data in Figures 6B, S6A, and S6F. This deviation makes the median value a potentially better descriptor of central tendency than the mean (See Supplemental Methods for details). Because Myo10 RNAi or LatA treatment has little or no effect on EB3 comet dissociation from paused MT plus ends, the EB3 cortical dwell time accurately reports MT-cortical interaction duration (Model 2).

(F) Increased contact frequencies of astral MTs with the cell cortex in LatA-treated or Myo10-depleted cells. Cortical contact frequencies were normalized by the mean of the control distribution acquired that day. The mean normalization value for the 5 pooled experiments was  $17.8 \pm 5.19$  MT cortical tracks per min (\*\*\* $p < 0.0005$ , permutation test of the means, 5 experiments).

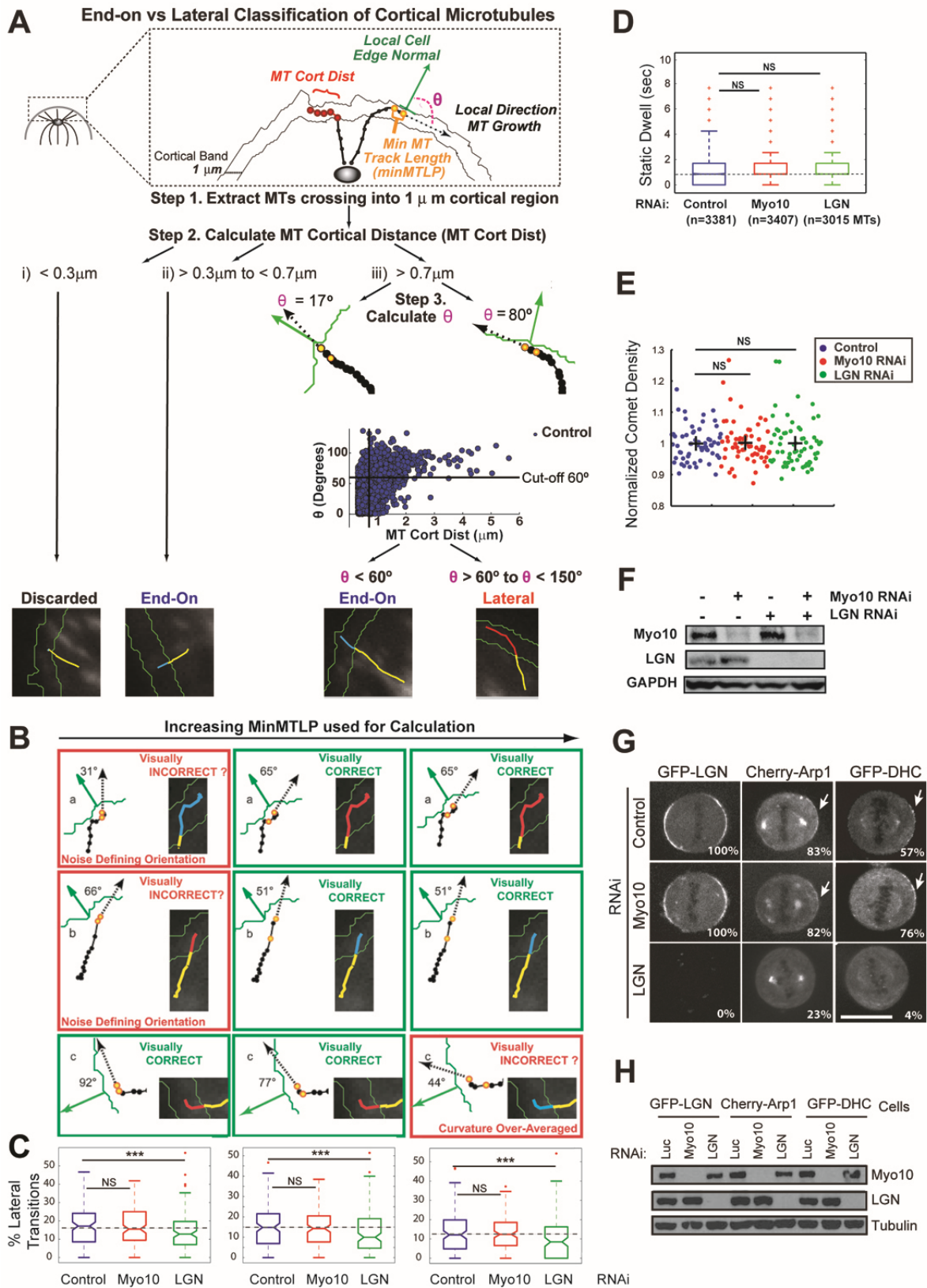


**Figure S7 (related to Figure 7). Effect of LGN/Dynein in Mediating the Transition from End-on to Lateral Microtubules during Anaphase Is Robust, Specific, and Differs from That of Myo10.**

(A) Scheme illustrating the automated algorithm to classify end-on and lateral cortical-microtubule (MT) capture. Note: The development of the algorithm necessitated implementing operational thresholds to distinguish the relevant categories of MT-cortical capture. However, we demonstrate that the conclusions are robust to small variation in the values for these thresholds (see below and the main text).

(Step 1) All astral MTs that crossed into the cortical band (1  $\mu\text{m}$  from cell edge) were identified and analyzed.

(Step 2) The distance traveled by the MT within the cortical region (termed, MT Cort Dist) was measured, and initial MT classifications were made based on this parameter. If the MT traveled  $< 0.3 \mu\text{m}$  within the cortical band, the interaction was considered to be insignificant and was not analyzed further. MTs that traveled between 0.3 and 0.7  $\mu\text{m}$  within the cortical band were considered to have significant cortical attachment. These interactions were considered to be end-on attachments by definition, because they fell below our threshold distance for lateral capture events. For MTs that traveled  $> 0.7 \mu\text{m}$  within the cortical band, we categorized lateral interactions based on the angle of movement relative to the cell edge.

(Step 3) To define the angle that MT ends move relative to the cell edge, we first identified the relevant track length for analysis, a parameter we termed the min MT Track Length parameter (minMTLP). The minimal track length that best discriminated lateral from end-on movement was defined empirically by matching the automated analysis to visual analysis. minMTLPs were then used to calculate the local direction of MT motion (dotted black vectors) relative to the direction perpendicular to the cell edge (termed the cell edge normal, green vectors). The resulting angle  $\Theta$  (the MT orientation relative to the cell edge) was then calculated. Comet trajectories with  $\Theta$ s  $< 60$  degrees (blue) were classified as “end-on” attachment, whereas those that were  $60 < \Theta < 150$  degrees (red), were classified as “lateral” attachments. The 60 degree cut-off for  $\Theta$  was set because it was the minimum angle observed for MTs that traveled long distances ( $> 3 \mu\text{m}$ ) within the 1  $\mu\text{m}$  cortical band (see the graph of  $\Theta$  versus MT Cort Dist).

(B-C) The conclusion that cortical dynein is required for the transition from end-on to lateral MT attachment is robust to modifications in the minMTLP threshold.

(B) We varied several parameters in the algorithm and found that the minMTLP had the most significant impact on our classification scheme (see Supplemental Methods). The minMTLP parameter determines the extent to which small displacements at the end of MT trajectories are considered to be significant. Three representative MT trajectories (named a, b, and c in the images) are shown, together with the classification that results when the minMTLP threshold is varied (216, 324, and 432 nm- left to right panels). Tracks are colored corresponding to their automated classification - end-on (blue) and lateral (red) - given the respective parameter settings. The specific MT track coordinates (minMTLP) used for calculation of the local MT orientation are highlighted as orange dots along the measured MT trajectory. MT classifications are boxed in green if marked “correct”, or in red if marked “incorrect”, by the experimentalist. The best correspondence between the automated analysis and manual curation of the data occurs with a minMTLP of 324 nm (middle panel). For MTs “a” and “b”, a smaller (216 nm) minMTLP resulted in more experimentalist-defined cortical MT classification errors (Left panels); this is intuitive because the magnitude of the MT displacement determining the local MT growth direction (red/blue) vectors is closer to the measurement noise. A longer minMTLP (432 nm) can also result in experimentalist-called errors (Right panel, microtubule “c”); in this case, the longer minMTLP, which requires the use of longer portions of the MT trajectory for the calculation of the local MT growth direction, can result in over-averaging that may obscure the measurement of potentially significant MT track curvature.

(C) The effect of cortical dynein on lateral cortical MT interaction is robust and is apparent even when the minMTLP is varied. Shown are box plots of the percent end-on to lateral transitions, calculated using the

indicated minMTPs (shown in B). Data were obtained with  $n > 100$  spindles poles per condition, from 4 experiments (Permutation test of the means,  $***p < 0.0003$ ).

(D) Neither Myo10 nor cortical dynein significantly decreases the static dwell time of MTs during anaphase in RPE-1 cells. The box plots show that the median anaphase cortical dwell time is unchanged by Myo10 RNAi or LGN RNAi (NS by permutation test of the medians). A comparison of the mean values did reveal a small ( $\sim 0.2$  sec) but significant difference [ $p < 0.001$ , permutation test of the means) (See Supplemental Methods for details)]. Note, this difference is not relevant to our conclusion, as it would suggest a slight increase in cortical dwell time, rather than a decrease. The difference between permutation tests of median and mean is related to some extreme outlier measurements in the distribution that make the mean value somewhat more variable in the re-sampling than the median.

(E) Depletion of Myo10 or LGN has no effect on the density of EB comets. A plot of EB comet density, normalized to the control, is presented (each data point: the average comet density from one cell).

(F) Western blots showing knockdown of Myo10, LGN, or both Myo10 and LGN by RNAi in the cells that are shown in Figure 7G.

(G-H) Cortical Dynein, Arp1 and LGN localization are not dependent on Myo10.

(G) Representative images showing that the localization of LGN, Arp1 and DHC as a lateral crescent (see arrows) at the cortex is unaffected by Myo10 RNAi (percentage of cells with polarized localization of cortical Dynein/LGN/Arp1 is indicated,  $\sim 50$  cells per condition from 2 experiments). Shown are HeLa cells that express GFP-LGN, Cherry-Arp1 and GFP-DHC. The positive control (LGN RNAi) produces the expected defects in the recruitment of cortical LGN, Arp1 and DHC. Scale bar, 10  $\mu\text{m}$ .

(H) Western blots showing efficient knockdown of Myo10 or LGN.

## LEGENDS TO SUPPLEMENTAL MOVIES

**Movie S1 (associated with Fig 1E):** Forced tripolar division by retraction fiber (RF) mediated forces. Control GFP-H2B-expressing U2OS cells with extra centrosomes were plated on Y-shaped FN patterns and imaged. The movie illustrates that RF-mediated pulling forces decluster extra centrosomes, pull them towards the sites where RFs are anchored to the matrix (tips of the “Y”), resulting in tripolar cell division (Kwon et al., 2008). Extra centrosomes were induced by transient Plk4 overexpression (Kleylein-Sohn et al., 2007).

**Movie S2 (associated with Fig 1E):** Bipolar division or randomly oriented cell division after Myo10 RNAi in a GFP-H2B-expressing U2OS cell with extra centrosomes on Y-shaped FN patterns. This movie illustrates that Myo10 is required to couple forces originating from RF regions to astral microtubules (MTs) that position centrosomes.

**Movie S3 (associated with Fig 5A):** Comparison of spindle pole movement relative to subcortical actin clouds in control, Myo10-depleted or CK-666 (Arp 2/3 complex inhibitor)-treated HeLa cells expressing GFP-Utr-CH and Cherry-tubulin. Three movies (control, Myo10-depleted and CK-666-treated cells) are concatenated into a single movie.

Control (time=00:00:03): Spindle pole movement towards subcortical actin clouds, after a short time lag, in control cells. This movie illustrates retraction fiber and actin cloud-mediated pulling forces on centrosomes during spindle oscillations.

Myo10 RNAi (time=00:00:11): Decreased spindle movement towards subcortical actin clouds after Myo10 RNAi. This movie illustrates that Myo10 is not required for assembly or dynamics of actin clouds, but is required for pulling forces from actin clouds to position centrosomes.

CK-666 treatment (time=00:00:19): Decreased spindle movement after CK-666 (Arp 2/3 complex inhibitor) treatment. This movie illustrates the requirement of actin clouds for centrosome positioning.

**Movie S4 (associated with Fig 6A-ii):** Growth and inferred shrinkage events of microtubules (MTs) analyzed with plusTipTracker. The movie shows an example of MT trajectories from a control GFP-EB3-expressing RPE-1 cell, illustrating how a microtubule shrinkage event (yellow dashed line) may be inferred from the linkage of two collinear EB comet trajectories (cyan solid lines). Top Panel: Raw images of GFP-EB3 detection (cyan crosses). Bottom Panel: EB3 comet detection (cyan crosses), plus trajectory overlays (cyan solid lines) of two collinear EB3 comet trajectories that were linked by the algorithm as having a high probability of belonging to the same microtubule. plusTipTracker follows the EB3 comets (crosses) along the trajectory during MT growth phase. Shown is an example where a catastrophe event followed by a rescue

event is inferred. Note in both panels the detection and tracking of the surrounding EB3 comets are not shown for clarity.

**Movie S5 (associated with Fig 7D):** The behavior of microtubules at the cortex in control, Myo10-depleted or LGN-depleted RPE-1 cells expressing GFP-EB3. Three movies have been concatenated.

Control (time=00:00:00): Two distinct modes of astral microtubule (MT) interaction with the cell cortex during anaphase. Left Panel: Using automated classification (Fig S7A and Supplemental Methods), all astral MT trajectories crossing into the 1  $\mu\text{m}$  cortical band (white overlays) are classified as end-on (blue) and lateral (red) cortical interactions; crosses mark the detected comet as it progresses along its MT track. The initial MT tracks, prior to entry into the cortical band, are plotted in yellow. Examples of high displacement MT trajectories ( $> 1.5 \mu\text{m}$ ) that start and end within the cortical band (red dashed lines) as well as MT trajectories that cross into the cortical band but traveling  $< 0.3 \mu\text{m}$  within the cortical region (white), are shown here for completeness, although they were excluded from the formal analysis. Only high confidence MT trajectories ( $> 5$  frames) are plotted. Right Panel: Raw images, including red arrow overlays that point to specific lateral MT transition events within the cortical band, as defined by our automated classification. All classifications were made using a Minimum Track Length parameter of 3 pixels ( $\sim 300 \text{ nm}$ , see Fig S7A).

Myo10 RNAi (time=00:00:24): Myo10 depletion does not affect the frequency of lateral cortical MT attachment during anaphase.

LGN RNAi (time=00:00:46): Inhibition of cortical dynein by LGN RNAi impairs lateral cortical MT attachment during anaphase.

## **EXTENDED EXPERIMENTAL PROCEDURES**

### **Cell Culture**

All cell lines were maintained at 37°C with 5% CO<sub>2</sub> atmosphere in DMEM (U2OS, HeLa, Utr-CH-GFP and tubulin-mCherry HeLa), DMEM:F12 (hTERT RPE-1), or DMEM:F12 medium without phenol red (H2B-mCherry RPE-1, EB3-GFP RPE-1), or DMEM medium without phenol red (H2B-GFP and H2B-mCherry U2OS, LGN-GFP HeLa, Arp1-mRFP HeLa, DHC-GFP HeLa). EB3-GFP RPE-1 cell line is a gift from W. Krek (Thoma et al., 2010). LGN-GFP HeLa, Arp1-mRFP HeLa, and DHC-GFP HeLa cell lines are gifts from I. Cheeseman (Kiyomitsu and Cheeseman, 2012). Media were supplemented with 10% FBS, 100 IU/ml penicillin and 100  $\mu\text{g}/\text{ml}$  streptomycin. The tetracycline-inducible U2OS cell line expressing Plk4 [a gift from E. Nigg, (Kleylein-Sohn et al., 2007)] was grown in DMEM supplemented with 10% of tetracycline-



free FBS, 100 IU/ml penicillin and 100 µg/ml streptomycin, 50 µg/ml hygromycin and 100 µg/ml G418. Plk4 expression was induced by addition of 2 µg/ml doxycycline for ~8-14 h.

### **siRNA and Plasmid Transfection**

RNAi experiments were conducted using the RNAi MAX transfection reagent (Invitrogen). Sequence information of the small interference RNA (siRNA) pools used from Dharmacon are as follows: human Myo10 set of 4 ON-TARGETplus MYO10 siRNA L-007217-00-0002, (J-007227-08) 5'-GGAGGAAAUUCAGGGAAU-3', (J-007217-07) 5'-GCGGGAGAAUUGUAGAUUA-3', (J-007217-06) 5'-CGUCGUAGCUGAUGUCUUA-3', (J-007217-05) 5'-GGACAUAAAUCUCAACUUG-3'; Human LGN/GPSM2 set of 4 ON-TARGETplus siRNA MU-004092-00-0002, (D-004092-01) 5'-GAACUACAGCACGACUUA-3', (D-004092-02) 5'-GAGAAUGGAUGAACAGAGA-3', (D-004092-03) 5'-CAGAUUAGAUGAUCAAAGA-3', (D-004092-04) 5'-GGGCAAUGCUUAAUUUCUAU-3'; human siGENOME Myo10-3'UTR siRNA D-007217-19-0005, 5'-CAACACUAAUCGACCGUAA-3'; human custom Myo10-5'UTR siRNA, 5'-UGGAGGAAGAAGAGACAAAUU-3'; human custom Myo10-5'UTR siRNA, 5'-UGAGGAACUUGGAGGAAGAUU-3'.

Plasmid transfection was carried out either using Lipofectamine 2000 (Invitrogen) for HeLa and U2OS cells or Neon Transfection System (Invitrogen) for RPE-1 cells, according to the manufacturer's protocol.

### **Drug Treatments**

50 µM PF573228 (Tocris Bioscience), or 25 µM PP2 (Calbiochem), were added 2 h after cell spreading, and maintained in culture for 24 h. Nocodazole (Sigma) was added at 10 µM for 4 h to completely depolymerize microtubules (MTs) for focal adhesion disassembly assays, and at 100 ng/µl for 6 h for mitotic arrest. Latrunculin A (Invitrogen) was used at 0.1, 0.5, or 1 µM, Blebbistatin (Sigma) at 1 µM, and Arp2/3 complex inhibitor CK-666 (EMD Millipore) at 100 µM, prior to imaging. MG132 (Calbiochem) was used at 20 µM for 2-3 h.

### **Immunofluorescence Microscopy**

Cells were plated on FN-coated coverslips or FN micro-patterned coverslips, as described (Kwon et al., 2008). For most experiments, to preserve Myo10, actin and retraction fiber morphology, cells were washed in pre-warmed PBS, and fixed in PBS containing 4% paraformaldehyde for 15 min at 37°C, followed by permeabilization in PBS-0.5% Triton X-100 for 15 min. To visualize cortical dynein and p150, cells were washed with PBS, pre-extracted with PBS-0.2% Triton X-100 for 30 sec at room temperature, and fixed in cold methanol at -20°C for 5 min. To visualize pFAK or centrin, cells were fixed in cold methanol at -20°C,

rehydrated in PBS, and treated with PBS-0.25% Triton X-100 for 5 min. After permeabilization, cells were immersed in blocking buffer (PBS containing 5% BSA and 0.1% Triton X-100) for 40 min, and incubated with primary antibodies at room temperature for 1 h, washed with PBS-0.1% Triton X-100 and incubated with fluorescence-conjugated secondary antibodies (1:1,000, Molecular Probes) or/and Alexa Fluor Phalloidin (1:250, Molecular Probes) at room temperature for 1 h. Cells were also stained for DNA with Hoechst 33342 (1:5,000, Invitrogen) in PBS and coverslips were mounted with ProLong Antifade mounting medium (Molecular Probes).

Images were acquired either by a Yokogawa CSU-22 spinning disk confocal mounted on a Zeiss Axiovert microscope (Zeiss) or by a Yokogawa CSU-X22 spinning disk confocal with Spectral Applied Research Borealis modification on a Nikon Ti inverted microscope (Nikon Instruments). A series of 0.5  $\mu\text{m}$  optical sections were acquired using x60 or x100 objective lens with an Orca ER CCD camera (Hamamatsu Photonics). Acquisition parameters, shutters, filter positions and focus were controlled by Slidebook software (Intelligent Imaging Innovations) or by MetaMorph 7 software (Molecular Devices).

### **Antibodies for Immunofluorescence**

Samples were incubated with primary anti-rabbit centrin2 (1:200, Santa Cruz), anti-rabbit pFAK (Y-397, 1:200, Invitrogen), anti-rabbit Myo10 (1:300, Novus Biologicals), anti-rabbit DHC (1:100, Santa Cruz Biotech. Inc), anti-mouse p150 (1:200, BD Transduction Laboratories), anti-mouse Paxillin (1:200, BD Transduction Laboratories), anti-mouse monoclonal  $\alpha$ -tubulin (DM1a, 1:500, Sigma), and anti-mouse monoclonal  $\alpha$ -tubulin (clone B-5-1-2, 1:3000, Sigma) antibodies.

### **Cell Adhesion Assay**

For the kinetics of FAK and Src activation, cells were trypsinized and replated on FN-coated plates [10 ng/ $\mu\text{l}$  as described, (Kwon et al., 2008)] to allow cell attachment. To avoid disturbing integrin-mediated adhesion signaling, cells were lysed directly in dishes while attached, at 1, 5, 18 h post-attachment.

Focal adhesion assays were performed as described (Ezratty et al., 2005). Briefly, serum-starved cells were grown on FN-coated coverslips, treated with 10  $\mu\text{M}$  nocodazole for 4 h to completely depolymerize MTs, washed with warm PBS three times, and released to regular medium for 1 h to allow MT repolymerization.

### **Long Term Live-cell Imaging**

Cells grown on glass-bottomed 12-well tissue culture dishes (Mattek) or in CYTOO chamber (CYTOO) were imaged on a Nikon Ti-E inverted microscope equipped with a precision motorized stage (Bioprecision, Ludl), and the Nikon Perfect Focus system enclosed within a temperature- and CO<sub>2</sub>-controlled environment that

maintained an atmosphere of 37°C and 5% humidified CO<sub>2</sub>. Images were captured at multiple points every 10 min for 2-3 days with a x20 objective and a cooled CCD camera (Coolsnap HQ2, Photometrics) controlled with NIS elements software (Nikon Instruments Inc.). Captured images from each experiment were analyzed using NIS-Elements software.

### **Immunoblotting**

Immunoblotting was carried out as described (Kwon et al., 2008). Samples were incubated with the primary antibodies: anti-rabbit FAK (1:4000, Cell Signaling), anti-rabbit pFAK (Y-397, 1:5000, Invitrogen), anti-rabbit pSrc (Tyr416, 1:1000, Cell Signaling), anti-rabbit Src (1:1000, Cell Signaling), anti-rabbit Myo10 (1:2000, Novus Biologicals), anti-rabbit Myo10 (1:5000, Sigma), anti-rabbit LGN (1:2000, Bethyl Laboratories, Inc.), anti-rabbit KIFC1 (1:1000, Proteintech), anti-rabbit mCherry (1:500, BioVison), anti-mouse GAPDH (1:240000, Ambion), anti-mouse GFP (1:12000, Roche Applied Science), and anti-mouse monoclonal  $\alpha$ -tubulin (DM1a, 1:15000, Sigma).

### **Plasmid Construction and Gene Replacement Experiments**

To generate N-terminal mCherry-tagged Myo10 constructs (mCherry-Myo10-pLenti-CMV-Puro), siRNA resistant versions of mCherry-Myo10 constructs were synthesized. The C-terminal 2.8 kb of Myo10 for wild type or 2.8 kb of KK-DD mutant or 2.2 kb of  $\Delta$ MyTH4 mutant were synthesized into pUC57-Amp (AgeI/HindIII) and the internal BglII site was removed by site-directed mutagenesis (Agilent Technologies). The N-terminal 3.4kb of wild-type Myo10 was subcloned into pUC57-Amp using BglII/AgeI upstream of the C-terminal fragments; the subsequent full length wild-type Myo10 or Myo10 KK-DD (6.2kb) or Myo10  $\Delta$ MyTH4 (5.6 kb) constructs were subcloned into pENTR mCherry C2, using BglIII/ HindIII. These constructs were transferred to pLenti- CMV-Puro DEST (Addgene#17452) via an LR clonase reaction. High titer lentivirus was prepared by concentrating the virus using PEG-it virus precipitation solution (System Biosciences), and was used to infect U2OS cells expressing GFP-H2B and Plk4 under the control of a tetracycline-inducible promoter.

For the centrosome clustering assays, U2OS cells expressing doxycycline (Dox)-inducible Plk4 (Kleylein-Sohn et al., 2007) were used to induce extra centrosomes; their clustering efficiency was assessed by scoring bipolar or multipolar divisions. U2OS cells expressing GFP-H2B or mCherry-H2B were subjected to two consecutive Myo10 3' UTR RNAi or to Myo10 ORF RNAi (J-007227-05, J-007227-06, J-007227-08) treatments, in order to deplete the endogenous protein. A double thymidine block was performed, as described (Kwiatkowski et al., 2010): thymidine for 18-20 h, release for 8-10 h with doxycycline induction of Plk4 during this time, then a second thymidine block, followed by release. For each experiment, the population of cells harboring extra centrosomes was assessed by two independent methods,

immunofluorescence microscopy to quantify centriole numbers, and live imaging of cells depleted of HSET to quantify spindle multipolarity induced by HSET RNAi (Kwon et al., 2008). In U2OS cells, HSET inhibition induces multipolarity in proportion to the fraction of cells with extra centrosomes.

For the knockdown-add-back rescue experiments (Fig S1B-G) to determine the effects of Myo10 constructs on centrosome clustering, cells expressing RFP-H2B were transfected with wild-type or mutant Myo10-GFP plasmids [gifts of R. Cheney, (Cox et al., 2002)] during the first thymidine release for additional 4 h (total of 12-14 h doxycycline induction), and 24 h prior to imaging. For lentiviral infection (Fig S3D), cells expressing GFP-H2B were infected with lentivirus containing wild-type or mutant Myo10- mCherry, as described above (total of 12-14 h doxycycline induction). For the rescue experiments of spindle orientation on FN-L patterns (Fig 3B), double thymidine block and lentivirus infection were performed, as described above without doxycycline treatment. Only cells that were positive for GFP-Myo10 or mCherry-Myo10 at comparable expression levels were subjected to quantitation, as gauged by the fluorescence intensity of Myo10 (NIS elements software). For measurements of mCherry-rescue protein expression level, the mean fluorescence intensity of mCherry was quantified from 20x20 pixel-square regions of cells.

### **Live Imaging of Subcortical Actin Clouds and Spindle Pole Movements**

HeLa cells were transfected with GFP-Utr-CH [a gift from W. Bement, (Woolner et al., 2008)] and GFP-positive cells were selected by fluorescence-activated cell sorting (FACS). FACS sorted cell clones were screened microscopically for optimal expression and visualization of actin clouds. These GFP-Utr-CH-expressing clones were then infected with an adenovirus containing mCherry-tubulin (gift of T. Wittmann) for 4 h. The double positive cells expressing GFP-Utr-CH and mCherry-tubulin were used for imaging within 7 days, a time interval during which mCherry-tubulin expression remains optimal. Cells were plated on 35 mm glass-bottomed tissue culture dishes (Mattek) and images were acquired at a single confocal plane where both poles are visible (mid-cortical plane) at 15 s intervals for 15 min using a x60 objective without binning.

### **High Resolution Live Cell Imaging for Microtubule Dynamics**

Clonal RPE-1 cells that stably express GFP-EB3 were plated on 35 mm FN-coated glass-bottomed tissue culture dishes (Mattek) and imaged at 37°C in DMEM-F12 phenol red free medium containing 10% FBS (Invitrogen).

To obtain images with high spatio-temporal resolution suitable for automated EB comet tracking and the extraction of parameters describing microtubule (MT) dynamics, cells were imaged at a single confocal plane for DIC and GFP. All images were collected with a Yokogawa CSU-X1 spinning disk confocal head with Spectral Applied Research Borealis modification on a Nikon Ti inverted microscope equipped with x60 Plan Apo NA 1.4 objective lens and Perfect Focus System. The microscope was enclosed in a custom-built

incubator at 37 °C and with 5% CO<sub>2</sub>. EGFP-EB3 fluorescence was excited with a 491nm solid state laser controlled with an ATOF, and emission was collected with a Semrock 405/491/561/642 multipass dichroic mirror and a Chroma 525/50 ET emission filter. Images were acquired every 0.75 sec for 100 time frames without binning, using a Hamamatsu ORCA ER cooled CCD camera controlled with MetaMorph 7 software (Molecular Devices).

Cells were imaged in the optical plane of horizontally positioned spindles, with both poles visible at the mid-cortex (i.e. corresponding to the position of subcortical actin clouds). Cell cycle stage for metaphase and post-anaphase cells were determined by the chromosome configuration from DIC images. To visualize lateral MTs in post-anaphase cells (Figs 7A-E, S7A-C) with similar pole-to-cortex distances (3-5 μm), cells were treated with 100 ng/μl of nocodazole for 6h, released to pre-warmed medium, and imaged during the 30-90 min window after release.

### **Statistical Methods for MT Dynamics and MT-cortex Interaction Measurements**

For all MT dynamics measurements (Figs 6B-D, S6A-C, S6F, S7E), we characterized cell-to-cell variability in the MT dynamics (for 7E, S7C, the data was analyzed per spindle pole). In Figures 6B, S6A-B, and S6F, to eliminate unavoidable systematic variation between daily experimental set-ups, each per cell MT dynamic value was normalized by the mean of the control cellular distribution for a given MT parameter obtained that day. Similarly, in Figure 6D, per cell MT values were normalized to the mean of the mCherry-WT cellular distribution. This normalization maintained consistency between Figures 6B and 6D, facilitating cross-comparison. For these cellular distributions, permutation tests were used to calculate statistical significance of changes in the mean between all conditions. Note, while a permutation test for differences in the means was always employed, as this test requires no assumptions regarding normality, this test will provide near identical results to a student's t-test if the dataset distribution does approach normality, which was typically the case for our per cell distributions.

In contrast, statistics related to cortical static dwell (Figs 6E, S7D) and the measurements of the EB3 dissociation rate from paused, non-cortical MTs (Fig S6E) were performed on pooled data from multiple cells. This was because the sample size that could be obtained per cell was limited (Sampled N in metaphase was 1-50 MTs per cell for the control condition). The data from these pooled samples deviated from normality to a greater extent than the per cell distributions (confirmed via Anderson-Darling tests), and contained some outliers, making the median value a potentially better descriptor of central tendency than the mean (see Legends to Figs S6E and S7D). A slight skew from outliers with long dwell times is in fact expected, given that longer dwell times are easier to measure than shorter dwell times with 0.85 second interval image acquisition. Therefore, the permutation test was used to calculate statistical significance of changes in the median between conditions in these cases. For all statistical comparisons related to the MT dynamics

parameter data the number of permutations for each permutation test was calculated based on sample size: maximum permutations = 10000 for very large sample sizes.

For box plots shown in Figures 6E, S6E, 7C, 7E, S7C, and S7D, the middle bar of the box indicates the median value of population, while the top and bottom bars indicate the 75<sup>th</sup> ( $q_3$ ) and 25<sup>th</sup> ( $q_1$ ) percentiles of the population. The extension of the whiskers is calculated as  $q_3 + 1.5(q_3 - q_1)$  and  $q_1 - 1.5(q_3 - q_1)$ , respectively. Data beyond the whiskers are shown as plus-signs (+) and may be considered as outliers to the distribution. However, in all our statistical tests, these values were included, as discussed above.

### **EB3 Comet Detection and Tracking**

Settings for detection and tracking of EB3-GFP comets for all conditions are as follows. The EB3 fluorescent comets for analysis of all MT dynamics were detected and tracked with use of a modified version of the plusTipTracker package (Applegate et al., 2011; Matov et al., 2010). Images were filtered using a difference of Gaussians, band-pass filter ( $\sigma_1 = 1$  pixel and  $\sigma_2 = 2$  pixels) to dampen both high and low frequency noise in the image and facilitate comet detection. Given the high density of the comets in mitotic cells, we used the watershed method for their detection (Applegate et al., 2011). The high concentration of EB3 decorated MTs within the spindle resulted in a tendency for EB3 mitotic images to display higher intracellular variance in fluorescence intensity than that seen for interphase cell images on which the package was developed (Applegate et al., 2011). Therefore, in this study the standard deviation of the intracellular background was estimated by fitting the first mode of the filtered intensity signals to a Gaussian function. Detection accuracy was verified manually and cells with poor detection were excluded from the data set. However, once the above modifications were made, detection problems were rare.

MT tracking parameters were set to be consistent for all conditions. Frame-to-frame linking parameters were set to a minSearchRadius of 2 pixels (216 nm) and a maxSearchRadius of 5 pixels (540 nm). MT growth tracks with a track length of less than 3 frames were discarded from further analysis.

The plusTipTracker software was designed to perform frame-to-frame linking of EB3 comet detections, and also to infer undecorated MT pause, shrinkage and undetected growth events by associating collinear, sequential growth sub-tracks (i.e. EB3 comet trajectories), which likely belong to the same MT, into compound tracks via a global optimization scheme (Applegate et al., 2011; Matov et al., 2010). MT growth subtrack linking parameters (i.e., “gap closing” parameters) were set as follows; maxForwardAngle = 30 degrees, maxBackwardAngle = 10 degrees, fluctuation radius = 2 pixels (216 nm), maximum shrinkage factor = 1.5, and maxGapLength = 12 frames (~10 secs). Forward subtrack linking was performed to both correct for occurrences wherein a comet might disappear temporally from the field of view, prematurely breaking the EB3 trajectory, as well as to identify MT pause events where the EB3 comet disassembles from the MT. These respective events can be identified based on the velocity of the gap linkage. Slow gap linkage

velocities more likely correspond to EB3 comet dissociation from the MT, whereas fast linkage velocities more likely correspond to EB3 bound MTs that leave the focal plane temporarily. Cut-offs for classifying fast forward subtrack linkages as undetected growth events were determined for each experimental day, and estimated via unimodal thresholding (Rosin, 2001) of the pooled forward gap speed distribution. Forward gap speeds above the threshold were considered undetected growth events, and interpolated MT growth coordinates were added to link the two MT growth subTracks. Forward gap speeds below the threshold were considered MT pause events, in which the EB3-comet dissociates from the MT due to an interruption in net MT polymerization, but does not exhibit measurable depolymerization (i.e. shrinkage). All backward subtrack linkages were classified as MT shrinkage events that were eventually 'rescued', transitioning back to EB3 associated MT regrowth at a spatial point along the first MT growth subtrack, behind the site of the original comet disappearance.

As documented previously (Applegate et al., 2011; Matov et al., 2010), one potential artifact in inferred shrinkage measurements corresponds to the false linking of very parallel moving MT tracks: mitotic cells tend to exhibit a higher number of very parallel MT tracks relative to interphase cells (for which the software was developed). Therefore, one may anticipate the frequency of backward links to increase when measuring shrinkage rates via plusTipTracker during mitosis. However, we expect that if the distributions corresponding to the local orientation of the candidate subtracks remained constant for all conditions tested, the probability of a linking artifact occurring would likewise remain constant, and thus not contribute to changes in the shrinkage rate observed among conditions. We measured the relative orientation of all pairs of candidate EB comet trajectories that fulfilled the backward linkage criteria and noted no statistically significant difference in this measurement among the perturbation conditions. We infer that the frequency of the artifact from parallel tracks was constant for all conditions tested, and therefore does not explain differences in shrinkage speed observed among the experimental conditions.

### **Measurements of Global Astral Microtubule Dynamics**

As described above, all RPE-1 cells for this analysis were imaged in the optical plane of the equator of horizontally positioned spindles. Estimation of the cell-edge for the astral region of interest was obtained from intensity thresholding of the EB3 GFP channel by rosin-based thresholding (Rosin, 2001). All masks were assessed visually for accuracy. Cells for which a visually acceptable mask could not be obtained via automated intensity thresholding were discarded from the analysis. In cases of significant cell-edge movement, the cell-edge masks were updated in each frame. These cell edge measurements were used in all cortical MT analyses requiring a cell edge estimate.

Non-astral (i.e. mitotic spindle) regions were delineated manually, and were subtracted from the whole cell region of interest, to obtain an astral specific mask. For each mitotic cell, all tracked astral MTs

were extracted using the `plusTipSubRoiExtractTracks` function in `plusTipTracker`. Only those EB3-decorated MT trajectories that exhibited at least 50 percent of their total lifetime within the astral region were included in the analysis; only those portions of the astral EB3 comet trajectories that fell within the astral region were used to calculate the lifetime and speed of the EB3-decorated MT trajectory; and only those shrinkage events that displayed 100 percent of their inferred coordinates within the astral subregion were included in the analysis.

To more directly monitor cell-to-cell heterogeneity following a given perturbation condition, we calculated the mean value for each of the MT parameters (EB3 comet speed, inferred MT shrinkage speed, and EB3 comet lifetime) for the astral MT distribution measured for each cell (~750 EB3 comet decorated MT trajectories and ~90 shrinkage events measured per cell). Because we observed subtle but significant fluctuations in the MT dynamics parameters of control cells from one experimental day to another, likely due to slight and unavoidable changes in the experimental conditions, we normalized the data to its respective daily experimental control population before pooling the data from different experimental days. For each experimental day corresponding to the RNAi or LatA treatment experiments (Fig 6B), the average of the per cell MT measurements for the control cells was calculated, and all per cell MT dynamics measurements for that day were divided by this value, such that all control normalized values scattered around a value of 1. In the case of the Myo10 depletion-add-back experiments (Figs 6D, S6C), a similar normalization procedure was employed using the values corresponding to the mCh-Myo10-WT (wild-type) add-back condition. This normalization allows a direct comparison of all add-back experiments with the data presented in Figures 6B-C and 6E (left panel).

### **Measurement of Per Cell Expression Level of Rescue Constructs**

To obtain a per cell estimate of Myo10 construct expression level in the MT dynamics rescue experiments, an automated procedure was developed where cell edge masks, obtained in the EB3 fluorescence channel, were used to collect the mean intra-cellular, background-subtracted fluorescence intensity in the mCherry channel. Extra-cellular background in mCherry signal was estimated per-frame by averaging the mCherry fluorescence intensity values in the extracellular region as defined from the cell edge mask. The background estimate was subtracted on a pixel-by-pixel basis from the raw intensity values. Negative pixel intensity values upon background subtraction were set to zero.

### **Clustering Cells with Similar Astral Microtubule Dynamics**

Calculations of the normalized mean for each MT parameter (EB3 comet speed, inferred MT shrinkage speed, and EB3 comet lifetime) per cell were collected for 5 experimental days (three days when cells were treated with control or Myo10 RNAi; two days when cells were treated with control or Myo10 RNAi, or with 0.5



$\mu\text{M}$  LatA), and were plotted in 3-dimensions, to assess whether cells that exhibit changes in one parameter (such as EB3 comet speed) likewise exhibit large stereotypical changes in the other two MT dynamics parameters (Fig 6B). The kmeans clustering function in Matlab R2012b (20 replicates, all other parameter set to default) was used to identify two groups of cells that exhibited similar MT dynamics behavior: the identities of cells in each cluster were obtained, and we calculated the percentage of cells from a given experimental treatment in each of the two MT dynamics clusters (Figs 6C-D, S6B). A permutation test of the means was likewise used to confirm the statistical significance of the difference between control and perturbation conditions for each of the three measured MT dynamics parameters (Figs S6A, S6C, EB3 decorated MT growth speed, inferred MT shrinkage speed, and EB3 decorated MT growth lifetime).

### **Cortical Region Creation and Microtubule Trajectory Extraction**

We used the `bwdist` function in Matlab 2012b to create a cortical region that was  $1.0\ \mu\text{m}$  from the cell edge, and extracted all measured EB3 bound microtubule (MT) trajectories that crossed into this cortical region from the non-cortical astral region of the cell (Figs 6E, 7A, S7A). MT trajectories were defined as those tracking measurements corresponding to an explicitly detected EB3-GFP comet (i.e. no inferred shrinkage or pausing behavior was considered in the cortical analysis); we reasoned that this definition was most consistent with previous studies that employed manual MT EB3 comet tracking. Only measured MT growth trajectories crossing once into the cortical region were considered for cortical calculations in this study, as these tracks are unequivocally from a single MT. To be considered a viable trajectory for analysis, the cortical MT trajectory likewise had to persist for more than 5 frames (3.4 sec).

### **Static Dwell Calculations**

Cortical classifications were first performed as described below (See Classification of End-on vs. Lateral MT Cortical Interactions section of Supplemental Methods) to classify all EB3 comet decorated MT trajectories that cross into the cortical region into either end-on or lateral growing MTs. Only tracks classified as end-on were used for the calculations of static dwell: we reasoned that MT dwell at the end of a laterally growing track likely represents a distinct molecular event. To calculate the time that the decorated MT was immobilized at the cortex, small masks with a diameter that was 2 pixels ( $\sim 216\ \text{nm}$ ) wide were made around the coordinate corresponding to each EB3 comet decorated trajectory endpoint (i.e. the point where the EB3 comet is no longer detected, either due to comet dissociation or due to the MT permanently leaving the focal plane of the image). The static dwell was calculated from the number of frames in which the EB3 comet centroid was detected within the respective local dwell mask (Fig 6E). Note that we excluded EB3 trajectory endpoint events where the EB3 signal disappeared and subsequently reappeared within the cortical band (See EB3 Comet Detection and Tracking section of Supplemental Methods for details regarding

detection/definition of these events). This is a distinct cortical event from EB3 decorated, MT persistence before catastrophe that we aimed to measure.

### **Measurements of Spindle Microtubule Growth**

EB3 comet intensity is extremely dense within the spindle region and the associated MTs exhibit much more complex dynamic behavior than the interphase data on which plusTipTracker was originally tested. In addition, optimization of the imaging conditions for EB3 comet detection and tracking in the astral region, our primary region of interest, often required saturating the pixels in the image corresponding to the spindle. These factors prevented the application of plusTipTracker to generate reliable EB3 trajectories in this region. Hence to test for the regional specificity of the MT dynamic changes in the Myo10 RNAi or LatA treatment condition to the astral region, kymograph analysis was employed.

For Kymograph analysis, the same data set where astral MTs were analyzed by plusTipTracker (Figs 6B-C) was used to generate GFP-EB3 kymographs to obtain MT growth speeds in both the spindle region and for the astral MTs (Fig S6D). For each cell, a kymograph was generated from a 2-pixel wide line drawn along the major axis of the spindle, encompassing the entire length of the cell. MT growth speeds were calculated by measuring the slopes of GFP-EB comet trajectories, as previously described (Stumpff et al., 2012; Tirnauer et al., 2002). Spindle MTs growing towards the equator and astral MTs growing toward the cell periphery were analyzed to measure MT growth speeds in the spindle and astral regions, respectively. Data were presented as distributions of individual MT growth speeds pooled from multiple cells per condition. The same results were obtained when all measurements from a single cell (for spindle and astral regions) were averaged to obtain a mean MT growth speed per cell for each region, and their distributions were compared in different conditions. Note that the kymograph analysis orthogonally validates the alterations in astral MT dynamics detected by plusTipTracker after Myo10-knockdown or LatA-treatment.

### **Estimation of EB3 Dissociation Rate**

We considered the possibility that the decreased cortical dwell time observed in Myo10 depleted or LatA-treated cells, as calculated via the EB3 marker, could be due solely to a faster dissociation rate of EB3 from the MT in these conditions (Fig S6E, Model 1), rather than reflecting a true decrease in the time the MT persists at the cortex before depolymerization (Fig S6E, Model 2). To test this possibility, we obtained an estimate for the global EB3 dissociation rate from a paused MT in different experimental conditions. To achieve this, MT pausing events that were accompanied by EB3 comet dissociation and followed by subsequent EB3-decorated MT regrowth were isolated using the plusTipTracker's 'gap closing' algorithm as described above (See EB3 Comet Detection and Tracking section of Supplemental Methods). These EB3 dissociation rate calculations were performed in precisely the same manner as the cortical dwell

measurements with the exception that, for cortical dwell measurements, only terminal EB3 trajectory endpoints or EB3 trajectory endpoints linked to a rescue event were considered (Fig S6E, upper panel). For EB3 dissociation rate analysis we considered the global population of paused MTs followed by regrowth assuming that effects of Myo10 depletion and LatA treatment on the kinetics of the comets would be the same throughout the cell.

### **Definition and Measurement of Mitotic Poles**

For all anaphase cells, coordinates for the two centrosomes were documented manually from the first frame of each movie, using the `impoint` function in Matlab 2012b; these two coordinates were used to calculate the long axis of symmetry corresponding to the cell. A single line perpendicular to this long axis of symmetry, and passing through the cell center, was used to define the pole-specific cortical regions for the analysis of the percent lateral transition (Figs 7D-E). We used the coordinates corresponding to the intersection between the long axis of symmetry and the edge of the cell mask in the first frame to calculate the pole to cortex distance ( $d$ ) with regard to each centrosome. As the pole-to-cortex distance is decreased, lateral MT events increased significantly; thus, all measurements of anaphase cortical MT parameters (Figs 7A-E) were obtained from spindle poles with a  $d$  of 3-5  $\mu\text{m}$  for all conditions.

### **Classification of End-on vs. Lateral Microtubule Cortical Interactions**

EB3-decorated microtubules (MTs) that travel short distances (MT Cort-Dist) within the cortical region (between 0.3  $\mu\text{m}$  and 0.7  $\mu\text{m}$ ) were designated *a priori* as perpendicular (“end-on”) MT events: we assumed that differences in orientation for these low-displacement tracks were likely due primarily to either noise or other factors that did not correspond to the more robust, potentially motor-driven, lateral sliding of interest [Fig S7A Step 2 (ii)]. EB3-decorated MTs traveling a distance (MT Cort-Dist) of less than 0.3  $\mu\text{m}$  in the cortical region were discarded from further analysis: we reasoned that these tracks did not contain enough cortex-specific-information to make a robust MT classification [Fig S7A Step 2 (i)]. EB3-decorated MTs traveling a distance (MT Cort-Dist) greater than 0.7  $\mu\text{m}$  within the cortical region were further filtered via their local orientation relative to the cell-edge, to assign them to either the lateral or perpendicular MT-cortical interaction class [Fig S7A Step 2 (iii)].

For each of the measured trajectories of MTs traveling a distance (MT Cort-Dist)  $> 0.7 \mu\text{m}$  within the 1  $\mu\text{m}$  cortical band, we calculated the local direction of MT motion at the very end of the measured MT trajectory (Fig S7A, dotted black vector). The specific coordinates of the measured MT trajectory used for this vector calculation were dictated by the Minimum MT Track Length parameter [minMTLP, (Figs S7A-B)]. As an EB3-decorated MT very often pauses at the cortex before comet-loss/ MT depolymerization, EB3 comets may exhibit small displacement fluctuations in their direction of movement, simply due to the noise

in the measurement. To prevent these noise-driven directional changes from dominating the local direction of MT motion measurement, detected coordinates were iteratively scanned backward in time along the measured MT trajectory until the Euclidean distance between the EB3 coordinate under question and the terminal MT trajectory coordinate was greater than or equal to the minMTLP (Fig S7A-B). Coordinates along each measured MT trajectory that fulfilled this distance criterion were then used to calculate the respective local direction of MT motion in the cortical region. Note that the minMTLP used for the local direction of MT motion calculations should be large enough to average out small changes in MT direction due to noise, but should be small enough so to not dampen the measurement of true MT track curvature corresponding to the lateral transitions that exhibit lower subsequent displacement (Fig S7B). We found that a minMTLP of approximately 3 pixels (324 nm) falls roughly within this category, as verified by manual classification of tracks by an experimentalist (Fig S7B, middle panels).

Once the direction of local MT motion was established for each MT, this value was used to calculate the orientation of movement of each cortical MT relative to the cell edge (Fig S7A step3). To make this calculation, we had to measure the local orientation of the cell edge: to this end, we found the point along the cell edge that was closest to the terminal coordinate of each MT trajectory. Coordinates of the cell edge within a radius of 10 neighboring pixels ( $\sim 1 \mu\text{m}$ ) centered on this point were extracted, and designated as the local cell edge for each corresponding MT. From these edge coordinates, the normal to local cell edge (green vectors, the direction perpendicular to the cell edge) was calculated with use of the princomp function in Matlab 2012b.

Using the above two vectors, we calculated the orientation of the MT relative to the local cell-edge normal ( $\Theta$ ). Those MTs with a local direction of MT motion forming an angle  $> 60$  degrees and  $< 150$  degrees with respect to the local cell edge normal (i.e. EB3 comets traveling approximately perpendicular to the cell edge normal and thus moving parallel to the cell edge), were designated as lateral MT trajectories (red in plots), whereas those MTs with a local direction of MT motion forming an angle  $< 60$  degrees with respect to the cell edge normal were designated as end-on MT trajectories (blue in plots). The value of 60 degrees was considered to be a reasonable cut-off for determining lateral transitions, as this was approximately the lowest orientation value exhibited by MTs that are traveling long distances within the  $1 \mu\text{m}$  cortical region (see scatter plots of MT track orientation vs. MT cortical displacement in Fig S7A). This behavior was consistent for all perturbation conditions tested.

### **Test for Robustness of Conclusions to Small Changes in Parameters**

We recognize that manual classifications are inherently subjective and that what constitutes a “correct”, biologically meaningful classification may slightly differ among individuals (Fig S7B). Therefore, while validation of the automated classifications against manual classifications is important, it is insufficient. The

power of a fully automated analysis lies in the fact that the criteria for classification can be standardized, and different definitions of a lateral MT interaction can be systemically explored. To this end, we varied the minimum MT track length used for the local MT orientation calculation, a parameter that dictates the degree to which small-displacement changes in the direction of MT motion at the very end of the measured MT trajectory are considered significant. (Figs S7A-B). We observed little change in the overall shape of the orientation vs. displacement distribution (scatter plots in Fig S7A) for the different choices of minimum MT track length parameter (minMTLP); based on this result, a cut-off of 60 degrees for the MT orientation relative to the cell edge was considered reasonable in all cases. As anticipated, increasing the minMTLP used to calculate the local MT orientation relative to the cell edge tended to decrease the absolute value of the percent lateral transitions per pole, as small changes in curvature at the end of the track were averaged; however despite this, the relative difference in the percentage of lateral transitions per pole observed among conditions tested was clearly maintained (Fig S7C).

## SUPPLEMENTAL REFERENCES

Cox, D., Berg, J.S., Cammer, M., Chingwundoh, J.O., Dale, B.M., Cheney, R.E., and Greenberg, S. (2002). Myosin X is a downstream effector of PI(3)K during phagocytosis. *Nat Cell Biol* 4, 469-477.

Kwiatkowski, N., Jelluma, N., Filippakopoulos, P., Soundararajan, M., Manak, M.S., Kwon, M., Choi, H.G., Sim, T., Deveraux, Q.L., Rottmann, S., *et al.* (2010). Small-molecule kinase inhibitors provide insight into Mps1 cell cycle function. *Nat Chem Biol* 6, 359-368.

Rosin, P.L. (2001). Unimodal thresholding. *Pattern Recognition*, 2083-2096.

Stumpff, J., Wagenbach, M., Franck, A., Asbury, C.L., and Wordeman, L. (2012). Kif18A and chromokinesins confine centromere movements via microtubule growth suppression and spatial control of kinetochore tension. *Dev Cell* 22, 1017-1029.

Thoma, C.R., Matov, A., Gutbrodt, K.L., Hoerner, C.R., Smole, Z., Krek, W., and Danuser, G. (2010). Quantitative image analysis identifies pVHL as a key regulator of microtubule dynamic instability. *J. Cell Biol.* 190, 991-1003.

Tirnauer, J.S., Canman, J.C., Salmon, E.D., and Mitchison, T.J. (2002). EB1 targets to kinetochores with attached, polymerizing microtubules. *Mol. Biol. Cell* 13, 4308-4316.